

High-Throughput Experimental Study of Wurtzite $Mn_{1-x}Zn_xO$ Alloys for Water Splitting Applications

Paul F. Ndione,^{*†} Erin L. Ratcliff,[‡] Suhash R. Dey,[§] Emily L. Warren,[†] Haowei Peng,[†] Aaron M. Holder,[†] Stephan Lany,[†] Brian P. Gorman,[†] Mowafak M. Al-Jassim,[†] Todd G. Deutsch,[†] Andriy Zakutayev,[†] and David S. Ginley[†]

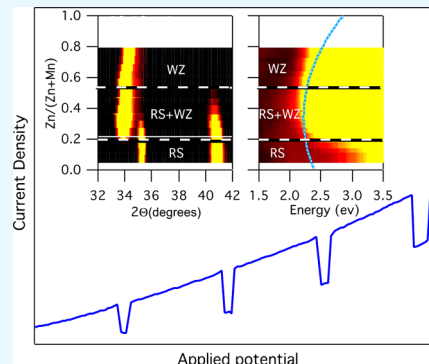
[†]Materials Science Center, National Renewable Energy Laboratory, Golden, Colorado 80401, United States

[‡]Department of Materials Science and Engineering, The University of Arizona, Tucson, Arizona 85721, United States

[§]Department of Materials Science and Metallurgical Engineering, Indian Institute of Technology Hyderabad, Kandi, Sangareddy, Hyderabad 502285, India

^{||}Department of Metallurgical and Materials Engineering, Colorado School of Mines, Golden, Colorado 80401, United States

ABSTRACT: We used high-throughput experimental screening methods to unveil the physical and chemical properties of $Mn_{1-x}Zn_xO$ wurtzite alloys and identify their appropriate composition for effective water splitting application. The $Mn_{1-x}Zn_xO$ thin films were synthesized using combinatorial pulsed laser deposition, permitting for characterization of a wide range of compositions with x varying from 0 to 1. The solubility limit of ZnO in MnO was determined using the disappearing phase method from X-ray diffraction and X-ray fluorescence data and found to increase with decreasing substrate temperature due to kinetic limitations of the thin-film growth at relatively low temperature. Optical measurements indicate the strong reduction of the optical band gap down to 2.1 eV at $x = 0.5$ associated with the rock salt-to-wurtzite structural transition in $Mn_{1-x}Zn_xO$ alloys. Transmission electron microscopy results show evidence of a homogeneous wurtzite alloy system for a broad range of $Mn_{1-x}Zn_xO$ compositions above $x = 0.4$. The wurtzite $Mn_{1-x}Zn_xO$ samples with the $0.4 < x < 0.6$ range were studied as anodes for photoelectrochemical water splitting, with a maximum current density of $340 \mu\text{A cm}^{-2}$ for 673 nm-thick films. These $Mn_{1-x}Zn_xO$ films were stable in pH = 10, showing no evidence of photocorrosion or degradation after 24 h under water oxidation conditions. Doping $Mn_{1-x}Zn_xO$ materials with Ga dramatically increases the electrical conductivity of $Mn_{1-x}Zn_xO$ up to $\sim 1.9 \text{ S/cm}$ for $x = 0.48$, but these doped samples are not active in water splitting. Mott–Schottky and UPS/XPS measurements show that the presence of dopant atoms reduces the space charge region and increases the number of mid-gap surface states. Overall, this study demonstrates that $Mn_{1-x}Zn_xO$ alloys hold promise for photoelectrochemical water splitting, which could be enhanced with further tailoring of their electronic properties.



INTRODUCTION

Photoelectrochemical (PEC) water splitting is one of the options for sustainable hydrogen production. Photoactive semiconductors are critical for the development of PEC water splitting technologies. In particular, the choice of an efficient n-type semiconductor photoanode material is a long-standing objective for PEC solar cell design. The key requirements for a single semiconductor to perform efficient water splitting can be summarized as follows: a band gap in the range of 1.5–2.0 eV (taking into account the 1.23 eV water dissociation energy and overpotential losses), band edge positions that straddle the water oxidation and reduction potentials, chemical and electrochemical stability in the operating environment under illumination, fast transport of the photogenerated carriers, high conversion efficiency, and low cost.^{1–5} Such moderate-band gap semiconductors can be also coupled with a suitable low-band gap semiconductor for

applications in PEC tandem solar cells that could potentially lead to higher solar-to-hydrogen conversion efficiencies.

Transition-metal oxides are promising candidates for water splitting because of their low cost and excellent stability in aqueous environments. However, many transition-metal oxides reported in the literature suffer from one of the following problems: their band gaps are too large for efficient light absorption, their band edges do not align with Nernst potentials for water oxidation/reduction, the materials are highly susceptible to chemical dissolution (especially under localized acidic conditions), and/or they exhibit poor semiconducting properties. For example, TiO₂ is the most widely studied photoelectrode material, but its wide band gap (~ 3 eV) severely limits its efficiency for PEC fuel generating

Received: November 30, 2018

Accepted: April 2, 2019

Published: April 24, 2019



applications unless interfaced with low-band gap semiconductors at either an anode or cathode.^{6–9} Exciting progress has been made over the past years on alternative binary oxide materials such as ZnO,¹⁰ WO₃,¹¹ Fe₂O₃,¹² Cu₂O,¹³ NiO,¹⁴ Ta₂O₅,¹⁵ Nb₂O₅,¹⁶ etc. However, most of these materials also suffer from intrinsic limitations for PEC applications, especially related to corrosion or to their band edges, which are not well aligned for the production of hydrogen. BiVO₄ has also shown promise as a photoanode material,¹⁷ but this material is still prone to photocorrosion and its performance is often limited by poor electron transport and by surface recombination.^{18–20} Therefore, new semiconductors need to be discovered and developed with specific functional attributes including band gap, band edge alignment, and improved transport properties.

Our computational research on d⁵ transition-metal oxides has shown the possibility of creating semiconducting manganese(II) oxide (MnO).²¹ This MnO compound can exist in the rock salt (RS) or wurtzite (WZ) structures. The WZ structure is metastable compared to the RS structure, which is the ground state. However, the RS structure presents a large band gap (3.5 eV) and self-trapping of holes, whereas the WZ structure is predicted to have an appropriate band gap (2.1 eV) for water splitting and band-like hole transport instead of hopping. Hence, the question arises on how to make MnO structurally stable in the wurtzite phase and therefore take full advantage of its properties for water splitting applications.

It is well known that the properties of a semiconductor can be tuned through alloying, that is, substitution of one element for another at tens of percent level. There are several reports in the literature on MnO doping in ZnO that focused on substitution of only a few percent of Mn for Zn. These studies focused mainly on the structural, electronic, and magnetic properties of thin films fabricated by sputtering,²² pulsed laser deposition,^{23–25} and molecular beam epitaxy.²⁶ However, there are only few reports with a particular emphasis on the alloying of MnO with ZnO and/or their application in water splitting. One experimental study²⁷ looked at the interaction of MnO and ZnO at different temperatures and pressures and determined the experimental conditions at which Mn_{1-x}Zn_xO (0.3 < x < 0.7) was formed in the rock salt structure. Another paper has reported on rock salt MnO:ZnO microflowers (5% of Mn ions in the ZnO matrix), finding that the emission of F⁺ centers at the oxygen vacancies could enhance the performance of the material in water splitting.²⁸ Other theoretical studies have demonstrated that MnO:ZnO alloys (Mn_{1-x}Zn_xO) could potentially be used for water splitting,^{29–32} reporting on tunability of the band gap,²⁹ efficiency of different n- and p-type dopants,³⁰ overpotential for water photo-oxidation on (001) surfaces,³¹ and their interfaces with water³² but all assuming the rock salt structure of Mn_{1-x}Zn_xO.

Our recent calculations showed that ZnO is a favorable candidate for stabilizing MnO in the wurtzite structure and this structure has promising properties for water splitting applications.³³ We predicted the band line up, dopability, and absorption in the visible region for wurtzite Mn_{1-x}Zn_xO. We also predicted the structure transition of Mn_{1-x}Zn_xO from RS to WZ (above x = 0.3) with favorable electron and hole transport properties and suitable physical properties for water splitting. This recently published theoretical work also includes some preliminary experimental results on wurtzite Mn_{1-x}Zn_xO alloys for water splitting.³³ In a more recent publication, we have also shown how this basic Mn_{1-x}Zn_xO work led to a new understanding of phase diagrams for heterostructural semi-

conductor alloys.³⁴ This new understanding offers a route for predicting the properties of other heterostructural semiconductor alloys and opens up opportunities in the development of new materials with desired functionalities.³⁵

In this paper, we present detailed results on the fabrication, characterization, and application of wurtzite Mn_{1-x}Zn_xO alloys for water splitting. We use high-throughput combinatorial synthesis, measurement, and analysis methodologies to rapidly screen the composition–structure–property relationships of Mn_{1-x}Zn_xO alloys and identify candidate samples for a more detailed study in PEC applications. TEM measurements are reported to demonstrate the homogeneity and structure of the fabricated alloys. Mott–Schottky measurements are used to determine the flat band potential, space charge layer, and carrier concentration of the samples. In addition, measurements of this material for water splitting applications are performed as a function of Zn atomic composition, pH, thickness, and Ga doping. These PEC measurements show that undoped samples exhibit a photoresponse current, while heavy doping inhibits the photoresponse due to decreased space charge layer and surface defect states suggested by photoemission spectroscopy.

RESULTS

Structural Properties. Depending on the substrate deposition temperature (T), oxygen partial pressure (pO₂), and chemical environment, the manganese oxide system can exist in a variety of oxidation states including MnO [Mn(II)], Mn₂O₃ [Mn(III)], Mn₃O₇ [Mn(II,III)], MnO₂ [Mn(IV)], MnO₃ [Mn(VI)], and Mn₂O₇ [Mn(VII)], with a number of possible polymorphs for each composition. However, the oxidation state for Mn we are interested in here is +2 as in MnO, since it is relevant to Mn_{1-x}Zn_xO alloys. Therefore, prior to depositing combinatorial libraries of Mn_{1-x}Zn_xO alloys, we need to identify the processing conditions that allow synthesizing MnO single-phase samples in the correct oxidation state. This is done by varying both the total pressure (P_{Total}) and the oxygen pressure (pO₂) during depositions as a function of the substrate temperature gradient obtained on a combinatorial heater. An analysis of the X-ray diffraction peaks allows the determination of various crystalline structures of known oxidation states as a function of pO₂, P_{Total}, and temperature.

A synthesis map determined from XRD patterns is presented in Figure 1, along with the representative XRD patterns of Mn–O in different oxidation states. A rock salt single-phase (face-centered cubic, JCPDS #07–0230) of MnO is obtained using a fixed P_{Total} of 5 mTorr and pO₂ of 10⁻⁵ Torr over a substrate temperature (T_S) range of 250–650 °C. The results show that a pO₂ < 10⁻⁵ Torr and P_{Total} < 5 mTorr are needed to grow rock salt MnO. A mixture of MnO and Mn₃O₄, pure Mn₃O₄, and a mixture of Mn₂O₃ and Mn₃O₄ appear successively as a function of P_{Total} and/or pO₂ increase. Single-phase ZnO (JCPDS #653411) was also obtained at the same condition as the single-phase MnO.

Experimental XRD maps for typical Mn_{1-x}Zn_xO alloy samples deposited at 381 and 519 °C and at different MnO concentrations are shown in Figure 2. Different crystalline phases are observed as a function of ZnO concentration at 381 °C, including rock salt (RS) at low x, wurtzite (WZ) at high x, and a mixture of RS and WZ at intermediate x. At x < 0.2, a shift of the (111) and (002) RS peak positions is observed with increasing ZnO composition (x), indicating that Zn ions

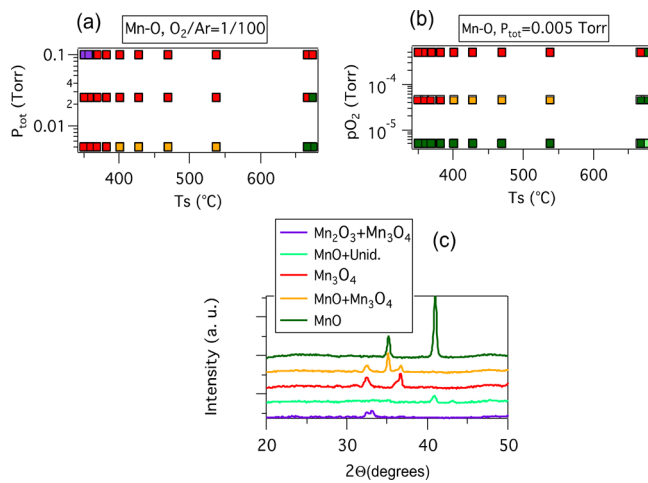


Figure 1. (a, b) Oxidation state maps obtained by XRD of the Mn–O system at (a) different total pressures as a function of substrate temperature and (b) different oxygen pressures as a function of substrate temperature. (c) Representative XRD patterns of the different phases, with the same color code as in (a) and (b). Note that the phase of interest, MnO, is in dark green.

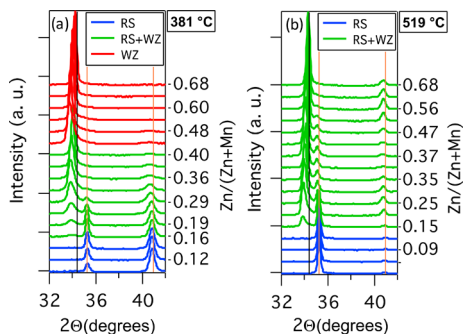


Figure 2. (a, b) XRD scans of Mn_{1-x}Zn_xO alloys with different x values deposited at (a) 381 °C and (b) 519 °C, leading to different rock salt (RS), wurtzite, (WZ), and mixture (WZ + RS) phases. The RS peaks at 35–36° (111) and 40–41° (200) and the WZ peak at 34–35° (002) are clearly visible.

substitute Mn sites without changing the RS crystal structure. The (002) WZ peak in the Mn_{1-x}Zn_xO alloy starts appearing at around $x = 0.2$ and coexists with the RS peaks up to $x = 0.2$. Substituting Mn with Zn at $x > 0.4$ caused a position shift of the (002) WZ peak to shift to higher angles. Correspondingly, the c -axis lattice constant of the wurtzite Mn_{1-x}Zn_xO alloy thin films is elongated with increasing Zn composition.

To determine the position of a phase boundary at a particular temperature on the Mn_{1-x}Zn_xO synthesis diagrams, we use the disappearing phase method. For example, the inset of Figure 3 shows an example of the use of the disappearing phase method to determine the RS/(WZ + RS) phase boundary at 260 °C. In this specific case, the phase boundary location in the Mn_{1-x}Zn_xO alloy is found at $x = 0.15$, where the WZ XRD peak intensity extrapolates to zero. The composition–temperature phase boundaries that correspond to the solubility limit of Mn in the WZ structure and Zn in the RS structure in Figure 3 are obtained by repeating the disappearing phase analysis at each studied temperature. From the synthesis phase diagram determined over the 180–520 °C temperature range, the solubilities of Mn in the WZ structure and Zn in the RS structure are found to decrease with

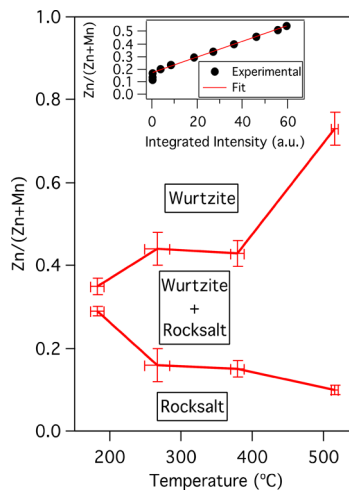


Figure 3. Mn_{1-x}Zn_xO system phase diagram between 180 and 520 °C. The inset illustrates the disappearing phase method used to determine the WZ/RS phase boundary at 260 °C.

increasing temperature. Hence, the width of the two-phase WZ + RS region (miscibility gap) increases with increasing temperature. From the thermodynamic point of view, this result may seem unusual, because the miscibility gap is expected to close with increasing temperature due to entropic contributions. This unexpected observation can be explained by kinetic limitations during the thin-film growth, where long-range phase separation is inhibited at low substrate temperatures (200–500 °C), as discussed in more detail in our previous works on Mn_{1-x}Zn_xO^{33,34} and related alloys.^{35–37}

The TEM analysis of the film microstructure is shown in Figure 4. Bright-field TEM imaging (Figure 4a) of the Mn_{0.48}Zn_{0.52}O film illustrates a uniform film thickness and columnar microstructure over the 20 μm-wide field of view analyzed in the FIB prepared cross section. As seen in the (01-10) dark-field image (Figure 4b) and the corresponding selected area diffraction pattern (Figure 4c), the grain structure of the Mn_{0.48}Zn_{0.52}O film is highly oriented toward (0001) with 10 to 30 nm grains rotated about this axis. The diffraction pattern also shows a single phase that indexes well to the wurtzite-type structure. High-resolution imaging of the film (Figure 4d) again illustrates the highly oriented film structure with grain rotations about the 0001 direction. Z-contrast scanning TEM (STEM) imaging was completed using a high-angle dark field (Figure 5a) of the film cross section, and the image illustrates no local changes in elemental distribution. The lack of changes in elemental chemistry is correlated by the EDS spectral image shown in Figure 5b. The quantitative analysis of the spectral image correlates well to the expected Mn_{0.48}Zn_{0.52}O stoichiometry and is consistent across the film thickness.

Optoelectronic Properties. It is important to evaluate the band gap of Mn_{1-x}Zn_xO from the measured absorption edge, because it helps define the efficiency of solar light absorption and therefore the upper limit of the photoconversion efficiency. As previously mentioned, a minimum of 1.23 eV per electron–hole pair generated is needed to drive the water splitting reaction. However, to account for the overpotential losses produced during the electron-transfer processes at the semiconductor/liquid junctions, an average of 2.0 eV is usually needed to drive the reaction.¹ Therefore, it is important for the

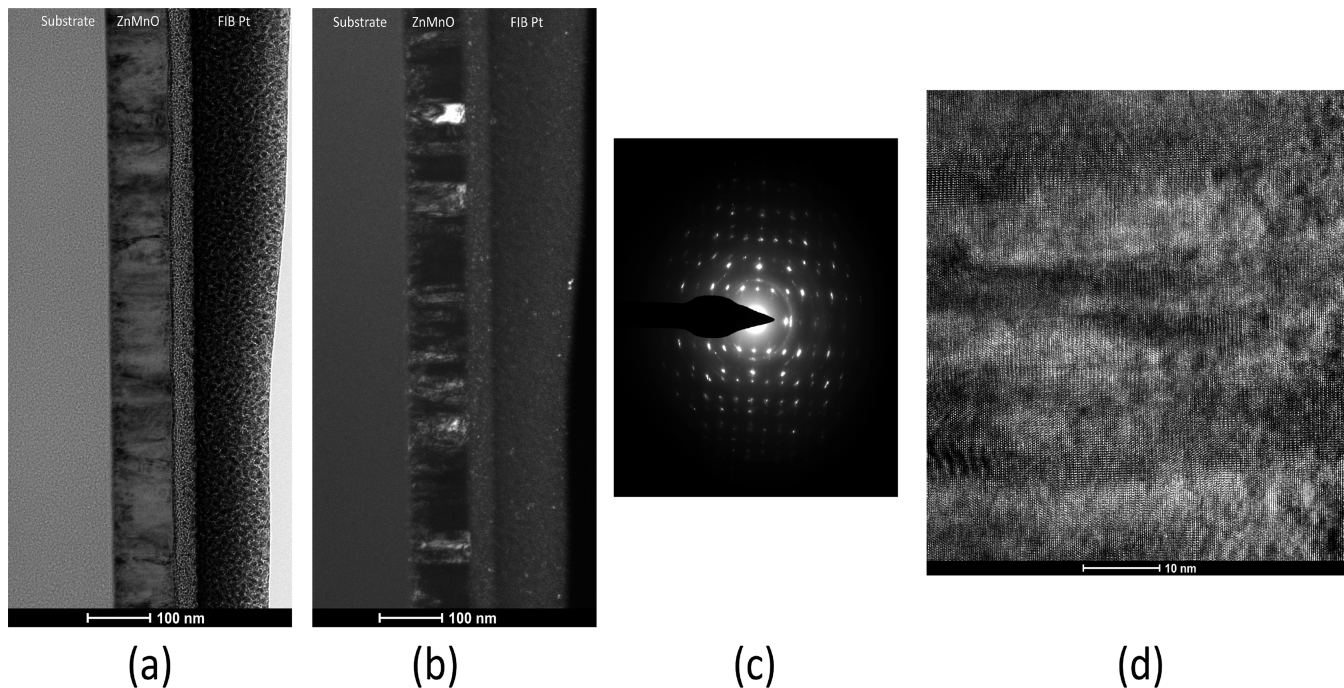


Figure 4. (a) Bright-field TEM analysis of the $\text{Mn}_{0.48}\text{Zn}_{0.52}\text{O}$ film microstructure illustrates a uniform film thickness and microstructure over the 20 μm -wide field of view analyzed in the FIB prepared cross section. As seen in the (01-10) dark-field image in (b) and the corresponding selected area diffraction pattern in (c), the grain structure of the $\text{Mn}_{0.48}\text{Zn}_{0.52}\text{O}$ film is highly oriented toward (0001) with 10 to 30 nm grains rotated about this axis. The diffraction pattern in (c) also shows a single phase that indexes well to wurtzite ZnO . (d) High-resolution imaging of the film again illustrates the highly oriented $\text{Mn}_{0.48}\text{Zn}_{0.52}\text{O}$ film structure with grain rotations about the 0001 direction.

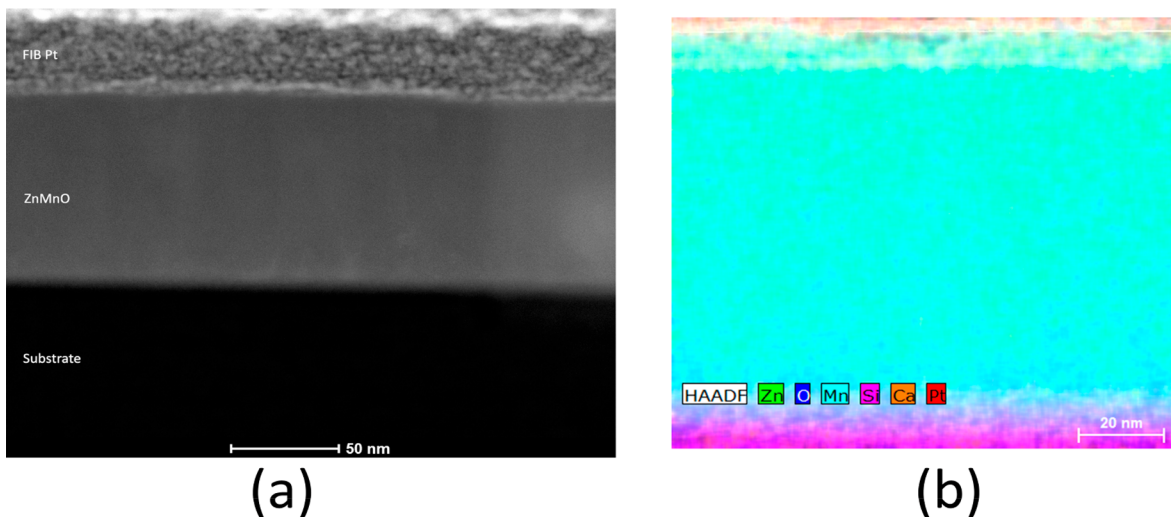


Figure 5. (a) Z-contrast scanning TEM (STEM) image of the $\text{Mn}_{0.48}\text{Zn}_{0.52}\text{O}$ film cross section illustrates no local changes in elemental distribution. The lack of changes in elemental chemistry is correlated by the EDS spectral image shown in (b). The quantitative analysis of the spectral image correlates well to the expected $\text{Mn}_{0.48}\text{Zn}_{0.52}\text{O}$ stoichiometry and is consistent across the film thickness.

band gap energy of $\text{Mn}_{1-x}\text{Zn}_x\text{O}$ to be around that value to efficiently split water.

The optical absorption spectra of the $\text{Mn}_{1-x}\text{Zn}_x\text{O}$ for different crystalline structures grown at 381 °C are shown in Figure 6. Substitution of Zn in MnO shifts the absorption edge toward the higher wavelength region, which indicates a decrease in the band gap energy. As-grown pure ZnO and MnO exhibit an absorption edge at around 3.3 eV. As x in the $\text{Mn}_{1-x}\text{Zn}_x\text{O}$ alloy increases, the optical band gap absorption edge of the alloys shows a redshift down to 2.1 eV for $x = 0.5$. The color intensity map of optical absorption spectra versus

Zn content in $\text{Mn}_{1-x}\text{Zn}_x\text{O}$ is shown in Figure 7 for several different synthesis temperatures. These absorption maps are also compared in Figure 7 with the corresponding XRD color intensity maps. We find that the abrupt change in the optical absorption onset occur at the RS/(RS + WZ) phase boundary, consistent with the appearance of the lower-band gap WZ phase. Furthermore, the Zn composition at which this abrupt change occurs decreases as a function of increasing synthesis temperature, which is consistent with the phase boundary results (Figure 3).

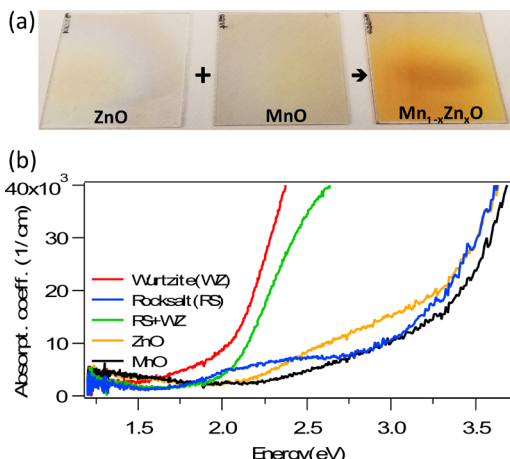


Figure 6. (a) MnO, ZnO, and $\text{Mn}_{1-x}\text{Zn}_x\text{O}$ thin films deposited on the glass. (b) Optical absorption spectra for different structures of grown $\text{Mn}_{1-x}\text{Zn}_x\text{O}$, ZnO, and MnO thin films.

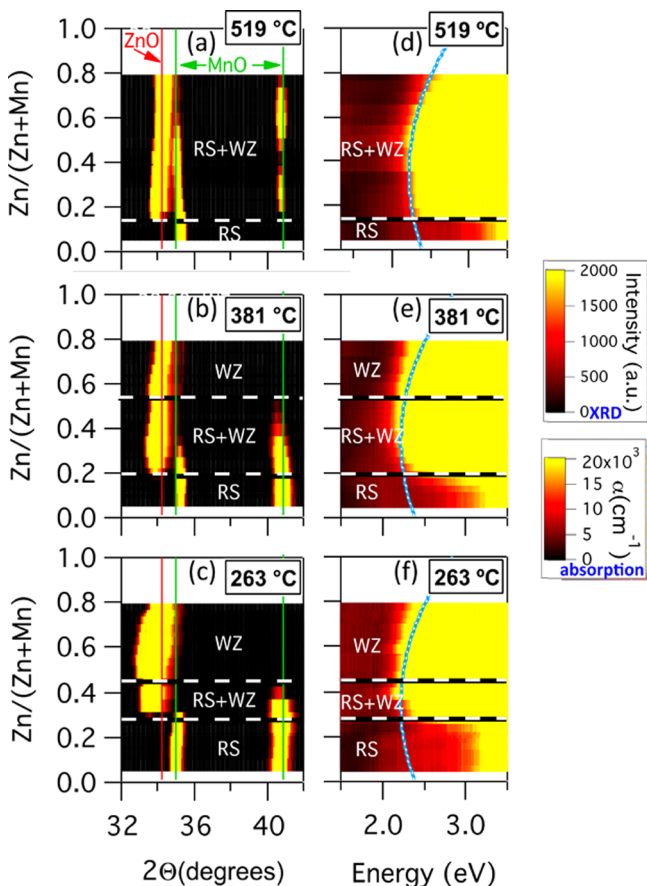


Figure 7. (a–c) 2D XRD diagram and (d–f) 2D band gap absorption onsets of $\text{Mn}_{1-x}\text{Zn}_x\text{O}$ at different temperatures as a function of composition. The blue dashed lines are theory predictions for the absorption onsets.

It has been found that the introduction of Mn^{2+} into the ZnO lattice leads to the presence of mid-gap states.²⁵ The mid-gap states may affect the measured absorption spectra and also influence the determination of the band gap.³⁸ However, in our case where Zn^{2+} is introduced into the MnO lattice, there is no evidence of the contribution of mid-gap states as the Zn content is increased in $\text{Mn}_{1-x}\text{Zn}_x\text{O}$. This is consistent with

what has been found in a previous work on undoped $\text{Mn}_{1-x}\text{Zn}_x\text{O}$.²⁹ However, the optical results are not sufficient to evaluate the presence of mid-gap states, and further studies using photoelectron spectroscopy are needed.

Most oxides photoanodes for photoelectrocatalytic water splitting in their intrinsic state suffer from poor electronic transport and therefore require doping with electric charge carriers. In this case, solar absorber materials should be n-type (electron carrier)-doped, and the minority (hole) carriers should have a long lifetime and high mobility. Therefore, we have explored the use of Ga as an extrinsic donor dopant for our $\text{Mn}_{1-x}\text{Zn}_x\text{O}$ system. Although it was reported that Ga will not contribute to the carrier or enhance the conductivity of rock salt $\text{Mn}_{1-x}\text{Zn}_x\text{O}$ alloys,³⁰ we have explored the use of extrinsic n-type doping by Ga because it is known as an efficient dopant in ZnO and wurtzite $\text{Zn}_{1-x}\text{Mg}_x\text{O}$ alloys.³⁹ In addition, our previous band structure calculations predicted a shallow Ga donor state with sufficiently low ionization energy to generate free electrons at room temperature.³³

As discussed in our previous publication,³³ doping was achieved for the PLD growth by using a ZnO target containing 4 cation % Ga. Thus, in the $\text{Mn}_{1-x-y}\text{Zn}_x\text{Ga}_y\text{O}$ alloys, the Ga doping level varies with the Zn composition x (i.e., $y_{\text{Ga}} = 0.04x$). Thus, the conductivity (in S/cm) was normalized by the Ga content per formula unit (i.e., per y_{Ga}). Note that the Ga content is 0.02 at the composition $x = 0.5$. As x and y in $\text{Mn}_{1-x-y}\text{Zn}_x\text{Ga}_y\text{O}$ increase, the conductivity increases from unmeasurable in the RS single-phase region ($x < 0.19$), to 10 S/cm/Ga within the miscibility gap ($0.19 < x < 0.45$), to 100 S/cm/Ga observed in the WZ single-phase region around $x = 0.5$, up to 10^4 S/cm/Ga approaching the pure ZnO composition typical of Ga:ZnO.⁴⁰ Subsequent Hall effect measurements have shown that $\text{Mn}_{1-x-y}\text{Zn}_x\text{Ga}_y\text{O}$ at $x = 0.48$ ($y_{\text{Ga}} = 0.02$) has an electron concentration of $n = 3 \times 10^{19} \text{ cm}^{-3}$ and mobility of $\mu = 0.4 \text{ cm}^2/(\text{V}\cdot\text{s})$, whereas at $x = 0.75$ ($y_{\text{Ga}} = 0.03$), $n = 1 \times 10^{20} \text{ cm}^{-3}$ and $\mu = 3.5 \text{ cm}^2/(\text{V}\cdot\text{s})$, consistent with conductivity values determined by a four-point probe. Interestingly, the work functions of the films measured by Kelvin probe microscopy were not greatly affected by the Zn content in the range in $\text{Mn}_{1-x}\text{Zn}_x\text{O}$ and by the doping concentration of Ga, perhaps due to the contribution of surface dipoles. The band gap of $\text{Mn}_{1-x}\text{Zn}_x\text{O}$ is also not expected to be affected by dilute Ga substitution in a few percent range, where rigid band approximation still holds and band filling effects are negligible.

DISCUSSION

After verifying the dopability of $\text{Mn}_{1-x}\text{Zn}_x\text{O}$ films without and with different Ga atom percentages (atom %) were fabricated for the photoelectrochemical experiments. In addition to the conductivity, the flat band potential of a photoanode is an important parameter to determine, as it reflects its ability to split water. Both conductivity and flat band potential help elucidate the band structure of a semiconductor when interfaced with a solution. Photoanodes drive the oxygen evolution reaction (OER) at the electrode–electrolyte interface. When the photoanode is illuminated with UV light, electrons and holes are generated, and the photoanode surface shifts the Fermi level of the bulk (measured potential) toward more cathodic potentials. The photogenerated minority carrier holes remain on the photoanode and migrate toward the surface to participate in the OER at the electrolyte interface by oxidizing water or hydroxide to liberate O_2 . The majority

carrier electrons are directed from the photoanode to the Pt catalytic cathode, where they reduce water or protons to form H₂ gas.

Mott–Schottky Analysis. In order to understand the intrinsic electronic properties of Mn_{1-x}Zn_xO in electrolyte solutions, we performed electrochemical impedance measurements in the dark. The carrier density and flat band potential (V_{fb}) at the photoelectrode/electrolyte interface can be quantified from the measured CV curves by the Mott–Schottky equation^{41,42}

$$1/C^2 = (2/e_0 \epsilon e_0 N_d)[(V - V_{fb}) - kT/e_0] \quad (1)$$

wherein e_0 is the electron charge, ϵ is the dielectric constant of Mn_{1-x}Zn_xO, ϵ_0 is the permittivity of free space, N_d is the donor density, V is the electrode applied bias, V_{fb} is the flat band potential, and kT/e_0 is the temperature-dependent correction term. In this equation, the area factor is included in the measured capacitance, as indicated by the F/cm² units in the corresponding plots (Figure 8). The high-frequency dielectric

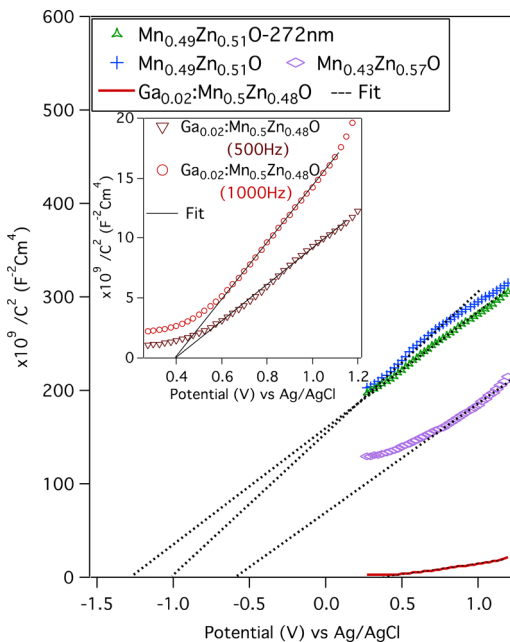


Figure 8. Mott–Schottky plots under dark conditions for Mn_{1-x}Zn_xO electrodes with different compositions, measured at 1 kHz in 0.1 M aqueous K₂SO₄ solution (pH 10). The dashed lines represent the extrapolated lines from the linear portion of the Mott–Schottky plots. The inset is the magnification of the Mott–Schottky plots under dark conditions for Ga_{0.02}:Mn_{0.5}Zn_{0.48}O at 0.5 and 1 kHz. All films are 132 nm-thick unless mentioned (data for the 272 nm-thick film is in green).

constant ϵ of Mn_{1-x}Zn_xO was theoretically (by independent particle approximation)⁴³ and experimentally (by spectroscopic ellipsometry) determined to be 4 and 4.7, respectively. We used here the experimental dielectric constant. The Mott–Schottky plots collected from different compositions of Mn_{1-x}Zn_xO alloys in PEC cells are presented in Figure 8. An extrapolation of the linear region (X intercept) in the Mott–Schottky plot ($1/C^2$ versus applied potential V) was used to determine the value of the flat band potential V_{fb} at 0.5 and 1 kHz. The positive slope indicates that Mn_{1-x}Zn_xO is an n-type material, consistent with Hall effect measurements.

The results for both the flat band potential and the carrier concentration determined for different Mn_{1-x}Zn_xO samples with x in the 0.4–0.6 range are presented in Figure 9. The

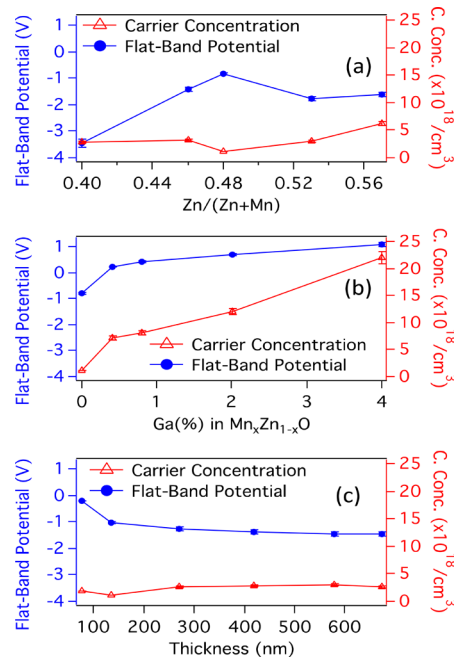


Figure 9. (a–c) Flat band potential (vs Ag/AgCl) and carrier concentration results as a function of (a) Zn atomic composition x in Mn_{1-x}Zn_xO, (b) Ga atom % doping in Mn_{1-x}Zn_xO, and (c) Mn_{1-x}Zn_xO film thickness.

carrier concentration of the undoped samples determined from the Mott–Schottky plot increased slightly with the Zn atomic concentration (Figure 9a). However, regardless of the Zn composition, the concentration is below 10¹⁹ cm⁻³. The carrier density of the samples increases with Ga doping with values varying between 10¹⁹ and 10²¹ cm⁻³ depending on the Ga atomic concentration (Figure 9b). It is worth noting that these carrier density values are in agreement with the results obtained from Hall effect measurements where the measured carrier densities for Ga-doped samples varied from 10¹⁹ and 10²⁰ cm⁻³. The variation of carrier density with Mn_{1-x}Zn_xO thickness is very small, indicating that the average concentration of donors does not vary much as the film becomes thicker (Figure 9c). However, if the total charge density does not vary, increasing the thickness should lead to an increase in the total amount of charges and therefore an increase in the flat band potential shift toward more cathodic potentials.^{44–46}

Photoelectrochemical Performance. The dependence of the PEC performance of Mn_{1-x}Zn_xO electrodes with 0.4 < x < 0.6 on the thickness is also studied, and the results are shown in Figure 10. The PEC performance of samples with thicknesses of 136 and 673 nm under chopped light with both front illumination (the Mn_{1-x}Zn_xO film facing the light) and rear illumination is shown in Figure 10a. All films exhibit an anodic photocurrent, indicating n-type behavior, and the photocurrent increases with the applied positive potential. The front- and back-illuminated current–voltage curves for the 136 nm sample strongly overlap each other, whereas for the 673 nm sample, they differ as discussed in our previous publication.³³ The inset of Figure 10a shows the generated photocurrent difference (in percentage) between the front and

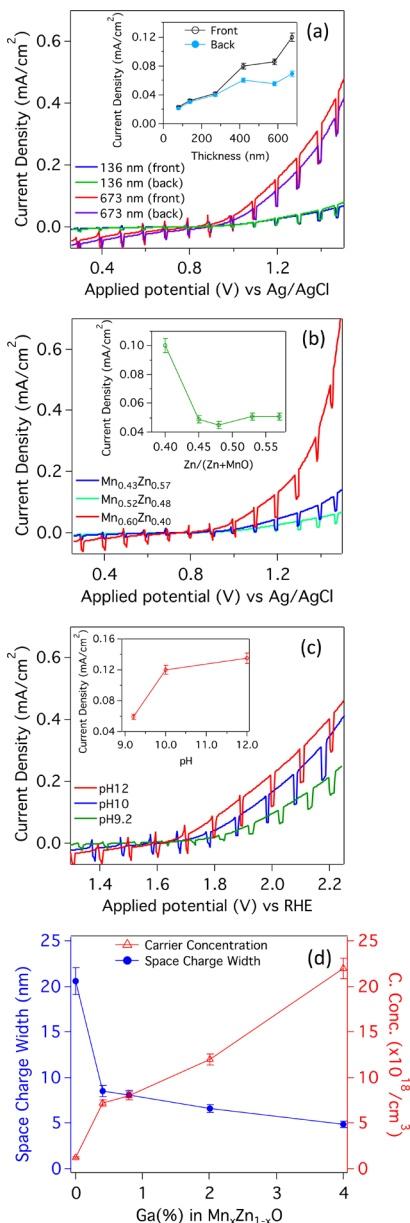


Figure 10. (a–c) Current density plots for $\text{Mn}_{1-x}\text{Zn}_x\text{O}$ as a function of applied potential for different (a) film thicknesses with front and back illumination in pH 10 (K_2SO_4) solution, (b) Zn atomic compositions for the 136 nm-thick film in pH 10 (K_2SO_4) solution, and (c) pH values for the 136 nm-thick film reported against RHE. (d) Carrier concentration and space charge width plot as a function of Ga atomic concentration in $\text{Mn}_{0.5}\text{Zn}_{0.5}\text{O}$ calculated using eq 3. The insets are current density plots of $\text{Mn}_{1-x}\text{Zn}_x\text{O}$ as a function of the (a) thickness for front and back illumination, (b) Zn atomic composition, and (c) pH.

back illumination (measured at ~ 1.25 V vs Ag/AgCl) for different photoelectrode thicknesses. For a thickness equal or lower than ~ 250 nm, a comparison between the front and back illumination shows an almost identical photoresponse. However, from a thickness equal to 200 nm or higher, this difference becomes obvious and more pronounced with the thickness. A larger photoresponse is observed when the material is illuminated from the front side. Under front-side illumination, most charge carriers are generated near the semiconductor/electrolyte interface where most of the light is

absorbed. This suggests that the performance of $\text{Mn}_{1-x}\text{Zn}_x\text{O}$ photoanodes for water splitting is not limited by the diffusion length of the photogenerated charge carriers for a film thickness equal or higher than 200 nm. For other oxide materials, the hole transport is the rate-limiting step for the PEC performance at much lower length scales.^{17,47,48}

The effect of the $\text{Mn}_{1-x}\text{Zn}_x\text{O}$ composition on the PEC performance was studied by varying x from 0.3 to 0.7. It was found (Figure 10b) that with an increase in x , the electrocatalytic activity first increases and then decreases. The highest $\text{Mn}_{1-x}\text{Zn}_x\text{O}$ PEC activity was obtained at $x = 0.4$, with the PEC activity dropping and remaining relatively flat past $x = 0.5$. The highest $\text{Mn}_{1-x}\text{Zn}_x\text{O}$ photoresponse, correlating with the lowest flat band potential (-3 eV) at $x \approx 0.4$ may be due to the lowest doping at this composition and hence the highest spatial extent of the built-in electric field at the liquid/semiconductor junction. Another potential explanation is the induced internal electric field close to the WZ/(RS + WZ) phase boundary that helps the electron–hole separation and thus enhances the photocatalytic activity of the mixed $\text{Mn}_{1-x}\text{Zn}_x\text{O}$ alloys.⁴⁹

The effect of the pH on the $\text{Mn}_{1-x}\text{Zn}_x\text{O}$ photocurrent was studied in different electrolyte environments of 0.1 M K_2CO_3 with pH 9.2, 0.5 M K_2SO_4 solution with pH 10, and a buffer salt (sodium phosphate tribasic + K_2SO_4) with pH 12. In order to compare the behavior of the $\text{Mn}_{1-x}\text{Zn}_x\text{O}$ material in an environment with different pH values, the applied potential was reported against the reversible hydrogen electrode (RHE) according to the Nernst equation

$$E_{\text{RHE}} = E_{\text{AgCl}} + 0.059\text{pH} + E_{\text{AgCl}}^0 \quad (2)$$

where E_{AgCl} is the experimental potential measured against the Ag/AgCl reference electrode and E_{AgCl}^0 is 0.198 mV (KCl saturated vs NHE) at 25 °C. The results shown in Figure 10c suggest that as the solution become more alkaline, the photocatalytic activities of $\text{Mn}_{1-x}\text{Zn}_x\text{O}$ substantially improves. Therefore, changing the pH has the opposite effect as varying the doping level of the semiconductor. A maximum photocurrent of $\sim 340 \mu\text{A cm}^{-2}$ was measured at pH = 12 for a 673 nm-thick film.

It is also worth noting that a direct contact of the $\text{Mn}_{1-x}\text{Zn}_x\text{O}$ photoanode with the K_2SO_4 electrolyte (pH = 10) for over 24 h under continuous UV illumination (simulated 1 sun illumination) did not show evidence of photocorrosion or degradation and did not substantially affect the measured current density values. Specifically, the current densities were 0.117, 0.115, 0.119 mA/cm² at 0, 7, and 25 h of measurement, which is within the $\pm 0.005 \text{ mA/cm}^2$ error of the technique. This observation is very encouraging for $\text{Mn}_{1-x}\text{Zn}_x\text{O}$ as a viable candidate material for PEC applications. However, it is worth mentioning that the Mn–O Pourbaix diagram is quite complex with multiple species and a range of oxidation states. On the other hand, the Zn–O Pourbaix diagram is rather simple, with ZnO being stable at pH = 10 in a wide range of potentials. Thus, one potential explanation for the $\text{Mn}_{1-x}\text{Zn}_x\text{O}$ stability is that a self-passivating ZnO layer is formed on the surface of $\text{Mn}_{1-x}\text{Zn}_x\text{O}$ alloys.

Regardless of the doping concentration, $\text{Mn}_{1-x}\text{Zn}_x\text{O}$ samples doped with Ga did not exhibit any photoresponse. This observation suggests that increased carrier concentration due to Ga doping may reduce the width of the space charge layer,

leading to less efficient separation of the photogenerated charge carriers. The width of the space charge layer (W) at the semiconductor/solution interface can also be derived from the Mott–Schottky plot relationship and be expressed as

$$W = [2\epsilon\epsilon_0(V - V_{fb})/e_0N_d]^{1/2} \quad (3)$$

As one can see in Figure 10d, the width of the space charge layer is reduced from 20 to 10 nm as Ga is introduced and from 10 to 5 nm as the Ga doping concentration is increased, which is consistent with the observed increase in carrier concentration. So, even for the undoped samples, 10^{19} cm^{-3} carrier density values obtained from the Mott–Schottky plots may be already too high for forming a wide depletion region in $\text{Mn}_{1-x}\text{Zn}_x\text{O}$ upon contact with the electrolyte, limiting the PEC performance. Therefore, additional Ga doping of the $\text{Mn}_{1-x}\text{Zn}_x\text{O}$ material can only further decrease the depletion width, which is detrimental to the performance of the material.

The lack of PEC activity for the Ga-doped $\text{Mn}_{1-x}\text{Zn}_x\text{O}$ samples may also result from several other effects. First, a very high doping concentration may lead to the dopants forming recombination centers and result into a rapid electron–hole recombination occurring before the electron and/or hole species have time to carry out catalytic reduction/oxidation.⁵⁰ Second, the specific surface area may decrease with the increase in Ga concentration that is unfavorable to obtain a high photocatalytic activity. Third, the band alignment of Ga-doped samples may not straddle the water redox potentials to drive the OER. To evaluate these different possibilities, additional measurements such as XPS and UPS may help better understand the effect of Ga doping on the PEC performance of $\text{Mn}_{1-x}\text{Zn}_x\text{O}$.

Photoemission Spectroscopy. Figure 11 shows ultraviolet photoelectron spectroscopy (UPS) data for wurtzite $\text{Mn}_{1-x}\text{Zn}_x\text{O}$ ($x \approx 0.5$) samples undoped and doped with 0.4 and 4% Ga. The data in Figure 11b show that there is a change in the O 2p orbital distribution in the He(I) spectra as a function of doping. Figure 11c gives a magnified view of the onset of occupied states, which were used to determine the ionization energy, as given in Table 1. Note that, here, we are investigating the O 2p σ orbitals are at ~ 4 eV and the O 2p π orbitals are at ~ 7 eV, rather than the electronic states of the electrode surface defined by the valence features, since a better way to understand these valence features is through a core-level analysis and connection with theories. The He(II) spectra (Figure 11d) show the increased sensitivity for the metal cation components of the valence band. This is evident in the comparison between the He(I) and He(II) spectra where Zn 3d orbital contributions emerge at ~ 11 eV below the Fermi level.

The UPS data presented in Figure 11 suggests that increasing the doping in wurtzite $\text{Mn}_{1-x}\text{Zn}_x\text{O}$ creates increased surface defects (mid-gap states) near the valence band, which can be observed in the tail states. Given the self-compensation, one can imagine similar tail states near the conduction band. The listed ionization energies (Table 1) are the onsets of the tail states, as shown in Figure 11c (zoomed in the region of the valence band from He(I)). The tail states also appear to correlate with changes in the distributions of the oxygen orbitals at 4–7 eV, which are most evident in the He(II) spectra (Figure 11d). This indicates that Ga causes a change to the valence surface states and local binding environment of the oxygen. In particular, the 4% Ga sample appears to have the

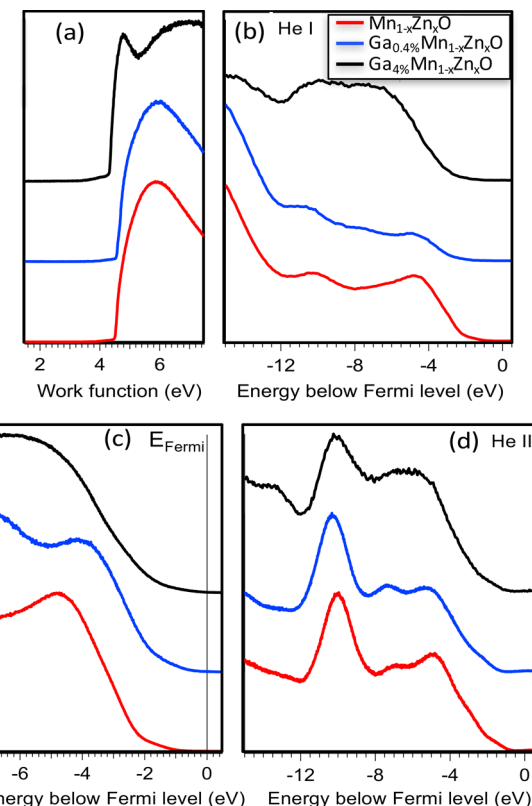


Figure 11. (a) Work function and (b–d) UPS spectra of $\text{Mn}_{1-x}\text{Zn}_x\text{O}$ samples ($x \approx 0.5$) with different doping concentrations of Ga as a function of kinetic energy induced by (b) He(I), (c) He(I) zoomed in the valence band region, and (d) He(II).

Table 1. Work Function, Ionization Energy (IE), and Fermi Level Relative to the Valence Band Minimum (ΔE) for Undoped and Doped $\text{Mn}_{1-x}\text{Zn}_x\text{O}$ ($x \approx 0.5$)

composition	work function	IE	ΔE
$\text{Mn}_{1-x}\text{Zn}_x\text{O}$ (undoped)	4.5	5.3	0.8
$\text{Mn}_{1-x}\text{Zn}_x\text{O}$ doped with 0.4% Ga	4.5	5.9	1.4
$\text{Mn}_{1-x}\text{Zn}_x\text{O}$ doped with 4.0% Ga	4.3	5.8	1.5

broadest distribution, which is consistent with doping. The mid-gap states are the most easily oxidized states and expected to be the first states to participate in the OER.⁵¹

In addition to light absorption (related to the band gap), the water oxidation efficiency also depends on two major factors: the probability and rate of charge carrier separation and transfer and the recombination rate of photogenerated electron–hole pairs. The mid-gap states play a role in both cases. They can act as intermediates for indirect charge transfer. In this case, the photogenerated carriers trapped in the mid-gap states predominantly initiate the water splitting process. However, the slow kinetics of the hole transfer to the water oxidation reaction leads to a low rate of reaction, which is detrimental to water splitting process.^{52–54} Instead of playing an intermediate role and without a chemical involvement with the water splitting reaction, the mid-gap states may act as trapping centers for photoexcited holes, preventing them to participate in the water splitting reaction by promoting the recombination of holes with electrons.^{55,56} Therefore, the mid-gap states contribute to lowering the rate of water oxidation. Although there is no consensus in the

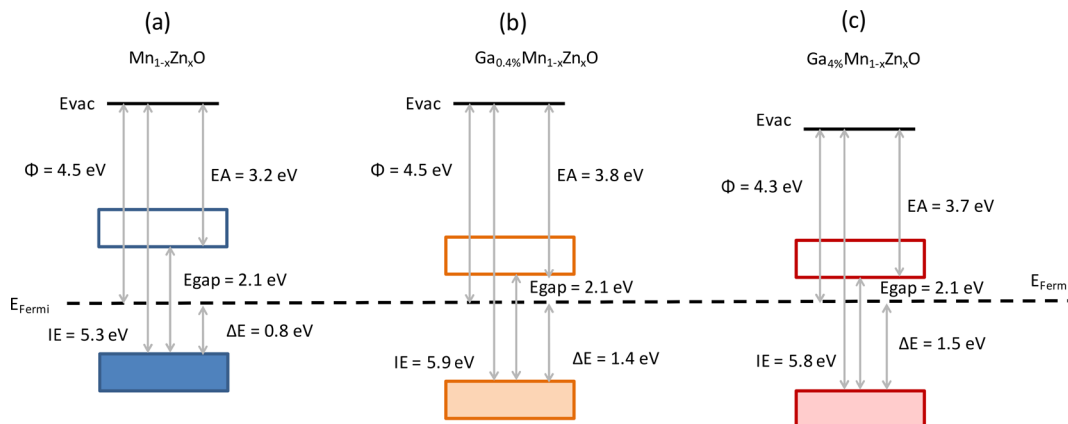


Figure 12. (a–c) Energy band diagrams of Mn_{1-x}Zn_xO ($x \approx 0.5$): (a) undoped, (b) doped with 0.4% Ga, and (c) doped with 4% Ga.

literature on which of these two processes is predominant, it is clear that both of them impede the photocatalytic reaction.

In an attempt to further understand the correlation between Ga concentrations and poor electrochemical behavior, we constructed a tentative band diagram of the doped Mn_{1-x}Zn_xO materials based on photoemission spectroscopy measurements. If we assume that the optical gap describes the energetic position of the conduction band, then we can conclude that increasing the Ga dopant increases the n-type character of the sample, as shown in the band diagrams in Figure 12. Specifically, as the Ga concentration increases, the Fermi level approaches the conduction band. However, the validity of such an assumption is questionable for the Mn_{1-x}Zn_xO sample. In Figure 12a, the Fermi level at the surface is closer to the valence band ($\Delta E \approx 0.8$ eV), indicating a p-type material. This result to first order appears as a direct contradiction to the n-type behavior demonstrated by Hall effect and Mott–Schottky measurements. This disparity could be explained by the fact that a bulk band gap may be very different at the surface. In addition, in the n-type material with defects, the Fermi level can be pinned at the surface at lower energy than in the bulk, leading to upward band bending and apparent lowering of the Fermi level measured by photoemission spectroscopy. However, assuming the same (surface) band gap, with increasing Ga concentration (Figure 12b,c), there is an increasing n-type surface character, consistent with bulk measurements. In the future, it may be interesting to compare this band diagram picture derived from photoemission measurements (Figure 12) to a similar picture that is constructed from photoelectrochemical measurements.

CONCLUSIONS

We used a high-throughput screening methodology to study Mn_{1-x}Zn_xO materials in a wide composition range (with x varying from 0 to 1) and identify a suitable composition for water splitting applications. The films were grown by combinatorial pulsed laser deposition. The observed band gap value E_{gap} of 2.1 eV at the $x \approx 0.5$ alloy composition is consistent with theory predictions for the WZ structure of the Mn_{1-x}Zn_xO alloy. The as-deposited films are insulating, and doping with Ga improved the conductivity of the films. The electrical conductivity for the 4% Ga-doped Mn_{1-x-y}Zn_xGa_yO alloy with $x = 0.48$ is 1.9 S/cm, with an electron concentration of $3.1 \times 10^{19} \text{ cm}^{-3}$ and mobility of $0.8 \text{ cm}^2/(\text{V}\cdot\text{s})$, consistent with Mott–Schottky measurements.

Mott–Schottky measurements were also used to determine the flat band potential and space charge width of all films and help evaluate the carrier concentration of undoped samples. Water splitting experiments have shown that as-deposited undoped films exhibit a photoresponse under illumination, while doped films with Ga do not produce any photocurrent. This could be explained by the small space charge region and the presence of mid-gap surface states. The maximum photocurrent density of $\sim 340 \mu\text{A cm}^{-2}$ was measured at pH 12 for a 673 nm-thick undoped film with $0.4 < x < 0.6$.

Overall, this study demonstrates that the Mn_{1-x}Zn_xO alloys are promising for photoelectrochemical water splitting but need further investigations and optimization to be considered as an efficient material. For instance, a careful control of the electron concentration is needed, with an appropriate trade-off between good transport properties, the absence of mid-gap states, and low recombination losses. Passivation of the mid-gap states or enhancing the OER rate by coupling Mn_{1-x}Zn_xO with an electrocatalyst can also help enhance the photoresponse. Regardless of these future challenges, Mn_{1-x}Zn_xO appears to be a stable and viable candidate for applications in PEC solar cells for hydrogen generation by water splitting.

METHODS

Materials Synthesis. Mn_{1-x}Zn_xO alloy thin films were grown on glass (Corning Eagle XG) substrates by pulsed laser deposition (PLD). We employed a thin-film high-throughput combinatorial approach^{57–64} to deposit “libraries” with a spatial gradient in both the composition and the substrate temperature. KrF excimer laser (Spectra-Physics) operating at 248 nm with a pulse duration of 25 ns was used. The laser was operated at 40 Hz, and the beam was focused through a 60 cm lens onto a commercial 1 inch MnO and ZnO rotating targets (purity 99.99%) at a 45° angle, with a laser fluence of 4 J/cm² on the target surface. The target-substrate distance was fixed to 7 cm. Prior to the depositions, the growth chamber was evacuated to a base pressure of 10⁻⁹ Torr using a turbomolecular pump then backfilled with an O₂/Ar mixture. In order to investigate the effects of different gas ratios and the total pressure, the O₂/Ar gas ratio was varied from 10⁻³ to 0.5 while keeping the total pressure (Ar + O₂) at 5 mTorr, and then the total pressure was varied from 5 to 100 mTorr. The deposition was performed at a substrate temperature ranging from 150 to 700 °C. A temperature gradient across the substrate was obtained by introducing a spacer between the holder and the substrate as reported elsewhere.⁶⁵ Films with a

lateral composition gradient were obtained by depositing sequentially from MnO and ZnO targets with a specific geometry with respect to the substrate.

Structural, Chemical, and Surface Characterizations.

Each of the combinatorial samples was automatically mapped at 44 points (4×11 grid) to find the properties of the material as a function of composition. X-ray fluorescence spectra were collected using a Matrix Metrologies MaXXi 5 with W anode, 800 μm collimator, and 300 s scan time. The resulting spectra were modeled using the MTF-FP software to obtain both the chemical composition and the thickness of the samples. The X-ray diffraction patterns of Cu K α radiation were collected using a Bruker D8 Discover. The diffraction peaks were assigned based on the MnO and ZnO reference diffraction patterns obtained from the Inorganic Crystal Structure Database (ICSD). Kelvin probe mapping with a 1 mm-diameter gold-coated probe was used to determine the work function of $\text{Mn}_{1-x}\text{Zn}_x\text{O}$ combinatorial samples. The samples were placed in ambient atmosphere and grounded during the work function measurements. The Kelvin probe mapping system was calibrated both before and after every mapping run using a highly oriented pyrolytic graphite standard with the reference 4.6 eV work function.

Optical and Electrical Characterizations. Optical spectra were mapped in the 300–2000 nm range using a fiber optics-based spectrometer with normally incident angle of light generated by deuterium and tungsten/halogen light sources and collected using Si and InGaAs detector arrays. The measured transmittance (T) and reflectance (R) spectra were converted into the absorption coefficient α using the relationship $\alpha = -\ln[T/(1 - R)]/d$, where d is the film thickness. The measurement of the electrical conductivity was carried out by using the four-point probe method. The current was applied by a Keithley 6221 DC and AC current source, and the voltage was measured with a Keithley 2182 voltmeter. Spectroscopic ellipsometry (J. A. Woollam M-2000S) was also used to both determine the dielectric functions and verify the thickness accuracy of the films.

Transmission Electron Microscopy. Specimens for transmission electron microscopy (TEM) investigations were prepared site-specifically in the combinatorial library using standard focused ion beam (FIB) thinning and in situ lift-out techniques. Specifically, an FEI Co. (Eindhoven, Netherlands) Nova 200 dual-column instrument operating at 5 keV electron energies was used to first identify a composition of $\text{Mn}_{0.48}\text{Zn}_{0.52}\text{O}$ and then protect the sample surfaces using electron beam-induced Pt deposition to a thickness of approximately 50 nm. A Ga ion accelerating voltage of 30 kV was used to further deposit a thicker layer of Pt and perform completion of rough milling and in situ extraction to a Cu grid. Final thinning was completed at 5 kV Ga ion accelerating voltages. Thinned specimens were subsequently examined in an FEI Co. Talos 200 FX (S)TEM operating at 200 keV. EDS spectral images (1000×1000 pixels) were acquired using a nominally 1.5 nA STEM probe at count rates up to 125 kcps using four windowless detectors. Spectral image analysis was completed using the Esprit v.1.9 software (Bruker Inc., Berlin, Germany). Quantification was completed using Cliff–Lorimer correction factors and fixing the oxygen concentration to 50 atom %, assumed from the stoichiometries of ZnO and MnO.

Photoelectron Spectroscopy. X-ray and UV photoelectron spectroscopy were performed on single-composition

films with a Kratos Axis Ultra X-ray photoelectron spectrometer with a monochromatic Al K α source (1486.6 eV) for XPS measurements and He(I) and He(II) excitation sources (21.2 eV and 40.8 eV, respectively) for UPS measurements, all at a base pressure of 10^{-9} Torr. Photoelectrons were collected in a hemispherical analyzer and detected with a photodiode array. A –10.00 V bias was applied to the sample to enhance the collection of the lowest kinetic energy electrons during UPS analysis. All UPS spectra were referenced to the Fermi level, E_F , of a clean polycrystalline gold substrate.

Photoelectrochemical (PEC) Experiments. Following all previous characterizations, single-composition $\text{Mn}_{1-x}\text{Zn}_x\text{O}$ samples for PEC characterizations were fabricated on the FTO substrate at the same conditions as for combinatorial samples, except the substrate deposition temperature that was fixed to 297 °C. For these samples, the Zn composition in $\text{Mn}_{1-x}\text{Zn}_x\text{O}$ was varied with $0.40 < x < 0.60$. The electrochemical measurements were performed using a CH Instruments 660A electrochemical analyzer with a conventional three-electrode system that consists of a platinum foil as a counter electrode, Ag/AgCl (saturated KCl) as a reference electrode, and $\text{Mn}_{1-x}\text{Zn}_x\text{O}$ (grown at 297 °C) on FTO glass substrates as the working electrode. The electrolytes used were 0.1 M K_2CO_3 with pH 9.2, 0.5 M K_2SO_4 solution with pH 10, and a buffer salt (sodium phosphate tribasic + K_2SO_4) with pH 12. A 250 W tungsten lamp solar simulator from Newport Instruments was used as a light source (calibrated to global AM1.5 intensity with a reference cell). The samples were illuminated through the back and front sides of $\text{Mn}_{1-x}\text{Zn}_x\text{O}$ photoelectrodes under chopped light. An insulating epoxy (Loctite Hysol 1C) was used to cover the entire $\text{Mn}_{1-x}\text{Zn}_x\text{O}$ sample except for the active area (between 0.27 and 0.42 cm^2). Electrochemical impedance measurements were performed in a 0.5 M K_2SO_4 carbonate buffer solution (pH 10) using an Impedance analyzer (Solartron SI 1260, Ametek, USA) and the same three-electrode system. A sinusoidal (AC) potential with an amplitude of 7 mV was superimposed on a bias voltage, and the measurements were carried out through systematic variation of the bias potential from 1.5 to 0.25 V versus Ag/AgCl at frequencies of 0.5 and 1 kHz. A scan rate of 5 mV/s was employed with a data acquisition rate of 5 s per point. The ZView software version 3.1c (Scribner Associates Inc., Southern Pines, NC, USA) was used for estimating the flat band potential and carrier concentrations through fitting the experimental data.

AUTHOR INFORMATION

Corresponding Author

*E-mail: paul.ndione@nrel.gov.

ORCID

Paul F. Ndione: 0000-0003-4444-2938

Erin L. Ratcliff: 0000-0002-2360-8436

Emily L. Warren: 0000-0001-8568-7881

Aaron M. Holder: 0000-0002-1878-1541

Andriy Zakutayev: 0000-0002-3054-5525

Notes

The authors declare no competing financial interest.

ACKNOWLEDGMENTS

This work was authored by the National Renewable Energy Laboratory, operated by Alliance for Sustainable Energy, LLC,

for the U.S. Department of Energy (DOE) under Contract No. DE-AC36-08GO28308. Funding was provided by the Office of Science (SC), Office of Basic Energy Sciences (BES), as part of the Energy Frontier Research Center “Center for Next Generation of Materials Design: Incorporating Metastability”. P.F.N. would like to thank Ethan Palay, Philip Parilla, John Perkins, and Bill Tumas from NREL for useful discussions. S.R.D. is thankful to Indo-US Science and Technology Forum for supporting his research stay at NREL under Bhaskara Advanced Solar Energy Fellowship (BASE 2014/F-8).

■ REFERENCES

- (1) Walter, M. G.; Warren, E. L.; McKone, J. R.; Boettcher, S. W.; Mi, Q.; Santori, E. A.; Lewis, N. S. Solar water splitting cells. *Chem. Rev.* **2010**, *110*, 6446–6473.
- (2) Stevanović, V.; Lany, S.; Ginley, D. S.; Tumas, W.; Zunger, A. Assessing capability of semiconductors to split water using ionization potentials and electron affinities only. *Phys. Chem. Chem. Phys.* **2014**, *16*, 3706–3714.
- (3) Hisatomi, T.; Kubota, J.; Domen, K. Recent advances in semiconductors for photocatalytic and photoelectrochemical water splitting. *Chem. Soc. Rev.* **2014**, *43*, 7520–7535.
- (4) Yin, W.-J.; Tang, H.; Wei, S.-H.; Al-Jassim, M. M.; Turner, J.; Yan, Y. Band structure engineering of semiconductors for enhanced photoelectrochemical water splitting: The case of TiO₂. *Phys. Rev. B* **2010**, *82*, No. 045106.
- (5) van de Krol, R.; Grätzel, M. *Photoelectrochemical Hydrogen Production*; 2012 edition (November 9, 2011) ed.; Springer: 2012; p 324.
- (6) Hernández, S.; Hidalgo, D.; Sacco, A.; Chiodoni, A.; Lamberti, A.; Cauda, V.; Tresso, E.; Saracco, G. Comparison of photocatalytic and transport properties of TiO₂ and ZnO nanostructures for solar-driven water splitting. *Phys. Chem. Chem. Phys.* **2015**, *17*, 7775–7786.
- (7) Fujishima, A.; Honda, K. Electrochemical photolysis of water at a semiconductor electrode. *Nature* **1972**, *238*, 37–38.
- (8) Didden, A.; Hillebrand, P.; Dam, B.; van de Krol, R. Photocorrosion mechanism of TiO₂-coated photoanodes. *Int. J. Photoenergy* **2015**, *2015*, 1–8.
- (9) Moniz, S. J. A.; Shevlin, S. A.; Martin, D. J.; Guo, Z.-X.; Tang, J. Visible-light driven heterojunction photocatalysts for water splitting – a critical review. *Energy Environ. Sci.* **2015**, *8*, 731–759.
- (10) Wolcott, A.; Smith, W. A.; Kuykendall, T. R.; Zhao, Y.; Zhang, J. Z. Photoelectrochemical study of nanostructured ZnO thin films for hydrogen generation from water splitting. *Adv. Funct. Mater.* **2009**, *19*, 1849–1856.
- (11) Cole, B.; Marsen, B.; Miller, E.; Yan, Y.; To, B.; Jones, K.; Al-Jassim, M. Evaluation of nitrogen doping of tungsten oxide for photoelectrochemical water splitting. *J. Phys. Chem. C* **2008**, *112*, 5213–5220.
- (12) Sivula, K.; le Formal, F.; Grätzel, M. Solar water splitting: progress using hematite (α -Fe₂O₃) photoelectrodes. *ChemSusChem* **2011**, *4*, 432–449.
- (13) Lim, Y.-F.; Chua, C. S.; Lee, C. J. J.; Chi, D. Sol-gel deposited Cu₂O and CuO thin films for photocatalytic water splitting. *Phys. Chem. Chem. Phys.* **2014**, *16*, 25928–25934.
- (14) Hu, C.; Chu, K.; Zhao, Y.; Teoh, W. Y. Efficient photoelectrochemical water splitting over anodized p-type NiO porous films. *ACS Appl. Mater. Interfaces* **2014**, *6*, 18558–18568.
- (15) Zhang, P.; Zhang, J.; Gong, J. Tantalum-based semiconductors for solar water splitting. *Chem. Soc. Rev.* **2014**, *43*, 4395–4422.
- (16) Hu, C.; Teoh, W. Y.; Ji, S.; Ye, C.; Iwase, A. In situ metal doping during modified anodization synthesis of Nb₂O₅ with enhanced photoelectrochemical water splitting. *AIChE J.* **2016**, *62*, 352–358.
- (17) Liang, Y.; Tsubota, T.; Mooij, L. P. A.; van de Krol, R. Highly improved quantum efficiencies for thin film BiVO₄ Photoanodes. *J. Phys. Chem. C* **2011**, *115*, 17594–17598.
- (18) Abdi, F. F.; Savenije, T. J.; May, M. M.; Dam, B.; van de Krol, R. The origin of slow carrier transport in BiVO₄ Thin film photoanodes: a time-resolved microwave conductivity study. *J. Phys. Chem. Lett.* **2013**, *4*, 2752–2757.
- (19) Liang, Y.; Messinger, J. Improving BiVO₄ photoanodes for solar water splitting through surface passivation. *Phys. Chem. Chem. Phys.* **2014**, *16*, 12014–12020.
- (20) Pilli, S. K.; Furtak, T. E.; Brown, L. D.; Deutsch, T. G.; Turner, J. A.; Herring, A. M. Cobalt-phosphate (Co-Pi) catalyst modified Mo-doped BiVO₄ photoelectrodes for solar water oxidation. *Energy Environ. Sci.* **2011**, *4*, 5028–5034.
- (21) Peng, H.; Lany, S. Semiconducting transition-metal oxides based on d⁵ cations: Theory for MnO and Fe₂O₃. *Phys. Rev. B* **2012**, *85*, 201202.
- (22) Lee, S.; Lee, H. S.; Hwang, S. J.; Shon, Y.; Kim, D. Y.; Kim, E. K. Effects of oxygen partial pressure during sputtering growth on physical properties of Zn_{0.93}Mn_{0.07}O thin films. *J. Cryst. Growth* **2006**, *286*, 223–227.
- (23) Tiwari, A.; Jin, C.; Kvitt, A.; Kumar, D.; Muth, J. F.; Narayan, J. Structural, optical and magnetic properties of diluted magnetic semiconducting Zn_{1-x}Mn_xO films. *Solid State Commun.* **2002**, *121*, 371–374.
- (24) Gilliland, S.; Segura, A.; Sánchez-Royo, J. F.; García, L. M.; Bartolomé, F.; Sans, J. A.; Martínez-Criado, G.; Jimenez-Villacorta, F. Absence of ferromagnetism in single-phase wurtzite Zn_{1-x}Mn_xO polycrystalline thin films. *J. Appl. Phys.* **2010**, *108*, No. 073922.
- (25) Johnson, C. A.; Kittilstved, K. R.; Kaspar, T. C.; Droubay, T. C.; Chambers, S. A.; Salley, G. M.; Gamelin, D. R. Mid-gap electronic states in Zn_{1-x}Mn_xO. *Phys. Rev. B* **2010**, *82*, 115202.
- (26) Jung, S. W.; An, S. J.; Yi, G.-C.; Jung, C. U.; Lee, S.-I.; Cho, S. Ferromagnetic properties of Zn_{1-x}Mn_xO epitaxial thin films. *Appl. Phys. Lett.* **2002**, *80*, 4561.
- (27) Sokolov, P. S.; Baranov, A. N.; Lathe, C.; Turkevich, V. Z.; Solozhenko, V. L. High-pressure synthesis of MnO-ZnO solid solutions with rock salt structure: in situ X-ray diffraction studies. *High Pressure Res.* **2011**, *31*, 43–47.
- (28) Sambandam, B.; Michael, R. J. V.; Manoharan, P. T. Oxygen vacancies and intense luminescence in manganese loaded ZnO microflowers for visible light water splitting. *Nanoscale* **2015**, *7*, 13935–13942.
- (29) Kanan, D. K.; Carter, E. A. Band gap engineering of MnO via ZnO alloying: a potential new visible-light photocatalyst. *J. Phys. Chem. C* **2012**, *116*, 9876–9887.
- (30) Kanan, D. K.; Carter, E. A. Ab initio study of electron and hole transport in pure and doped MnO and MnO:ZnO alloy. *J. Mater. Chem. A* **2013**, *1*, 9246–9256.
- (31) Kanan, D. K.; Keith, J. A.; Carter, E. A. First-Principles modeling of electrochemical water oxidation on MnO:ZnO(001). *ChemElectroChem* **2014**, *1*, 407–415.
- (32) Kanan, D. K.; Keith, J. A.; Carter, E. A. Water adsorption on MnO:ZnO(001) — From single molecules to bilayer coverage. *Surf. Sci.* **2013**, *617*, 218–224.
- (33) Peng, H.; Ndione, P. F.; Ginley, D. S.; Zakutayev, A.; Lany, S. Design of Semiconducting Tetrahedral Mn_{1-x}Zn_xO Alloys and Their Application to Solar Water Splitting. *Phys. Rev. X* **2015**, *5*, No. 021016.
- (34) Holder, A. M.; Siol, S.; Ndione, P. F.; Peng, H.; Deml, A. M.; Matthews, B. E.; Schelhas, L. T.; Toney, M. F.; Gordon, R. G.; Tumas, W.; Perkins, J. D.; Ginley, D. S.; Gorman, B. P.; Tate, J.; Zakutayev, A.; Lany, S. Novel phase diagram behavior and materials design in heterostructural semiconductor alloys. *Sci. Adv.* **2017**, *3*, No. e1700270.
- (35) Siol, S.; Holder, A.; Steffes, J.; Schelhas, L. T.; Stone, K. H.; Garten, L.; Perkins, J. D.; Parilla, P. A.; Toney, M. F.; Huey, B. D.; Tumas, W.; Lany, S.; Zakutayev, A. Negative-pressure polymorphs made by heterostructural alloying. *Sci. Adv.* **2018**, *4*, No. eaao1442.
- (36) Han, Y.; Holder, A. M.; Siol, S.; Lany, S.; Zhang, Q.; Zakutayev, A. Zinc-Stabilized Manganese Telluride with Wurtzite Crystal Structure. *J. Phys. Chem. C* **2018**, *122*, 18769.
- (37) Siol, S.; Han, Y.; Mangum, J.; Schulz, P.; Holder, A. M.; Klein, T. R.; van Hest, M. F. A. M.; Gorman, B.; Zakutayev, A. Stabilization

- of wide band-gap p-type wurtzite MnTe thin films on amorphous substrates. *J. Mater. Chem. C* **2018**, *6*, 6297.
- (38) Fukumura, T.; Jin, Z.; Ohtomo, A.; Koinuma, H.; Kawasaki, M. An oxide-diluted magnetic semiconductor: Mn-doped ZnO. *Appl. Phys. Lett.* **1999**, *75*, 3366.
- (39) Ke, Y.; Lany, S.; Berry, J. J.; Perkins, J. D.; Parilla, P. A.; Zakutayev, A.; Ohno, T.; O'Hayre, R.; Ginley, D. S. Enhanced electron mobility due to dopant-defect pairing in conductive ZnMgO. *Adv. Funct. Mater.* **2014**, *24*, 2875–2882.
- (40) Bhosle, V.; Tiwari, A.; Narayan, J. Metallic conductivity and metal-semiconductor transition in Ga-doped ZnO. *Appl. Phys. Lett.* **2006**, *88*, No. 032106.
- (41) Gelderman, K.; Lee, L.; Donne, S. W. Flat-band potential of a semiconductor: using the Mott–Schottky equation. *J. Chem. Educ.* **2007**, *84*, 685–688.
- (42) Turner, J. A. Energetics of the semiconductor-electrolyte interface. *J. Chem. Educ.* **1983**, *60*, 327–329.
- (43) Paier, J.; Marsman, M.; Kresse, G. Dielectric properties and excitons for extended systems from hybrid functionals. *Phys. Rev. B* **2008**, *78*, 121201.
- (44) Dukštinė, N.; Sinkevičiūtė, D. Photoelectrochemical properties of MoO₂ thin films. *J. Solid State Electrochem.* **2013**, *17*, 1175–1184.
- (45) Jun, K.; Lee, Y. S.; Buonassisi, T.; Jacobson, J. M. High photocurrent in silicon photoanodes catalyzed by iron oxide thin films for water oxidation. *Angew. Chem. Int. Ed. Engl.* **2012**, *51*, 423–427.
- (46) Park, K. J.; Parsons, G. N. Bulk and interface charge in low temperature silicon nitride for thin film transistors on plastic substrates. *J. Vac. Sci. Technol., A* **2004**, *22*, 2256–2260.
- (47) Zhang, L.; Reisner, E.; Baumberg, J. J. Al-doped ZnO inverse opal networks as efficient electron collectors in BiVO₄ photoanodes for solar water oxidation. *Energy Environ. Sci.* **2014**, *7*, 1402–1408.
- (48) Liang, Y.; Enache, C. S.; van de Krol, R. Photoelectrochemical characterization of sprayed α -Fe₂O₃ thin films: influence of Si doping and SnO₂ interfacial layer. *Int. J. Photoenergy* **2008**, *2008*, 1–7.
- (49) Ju, M.-G.; Wang, X.; Liang, W.; Zhao, Y.; Li, C. Tuning the energy band-gap of crystalline gallium oxide to enhance photocatalytic water splitting: mixed-phase junctions. *J. Mater. Chem. A* **2014**, *2*, 17005–17014.
- (50) Lin, M. Z.; Chen, H.; Chen, W. F.; Nakaruk, A.; Koshy, P.; Sorrell, C. C. Effect of single-cation doping and codoping with Mn and Fe on the photocatalytic performance of TiO₂ thin films. *Int. J. Hydrogen Energy* **2014**, *39*, 21500–21511.
- (51) Pyper, K. J.; Yourey, J. E.; Bartlett, B. M. Reactivity of CuWO₄ in photoelectrochemical water oxidation is dictated by a midgap electronic state. *J. Phys. Chem. C* **2013**, *117*, 24726–24732.
- (52) Young, K. M. H.; Klahr, B. M.; Zandi, O.; Hamann, T. W. Photocatalytic water oxidation with hematite electrodes. *Catal. Sci. Technol.* **2013**, *3*, 1660–1671.
- (53) Zandi, O.; Hamann, T. W. Determination of photoelectrochemical water oxidation intermediates on haematite electrode surfaces using operando infrared spectroscopy. *Nat. Chem.* **2016**, *8*, 778–783.
- (54) Ding, C.; Shi, J.; Wang, Z.; Li, C. Photoelectrocatalytic water splitting: significance of cocatalysts, electrolyte, and interfaces. *ACS Catal.* **2016**, *7*, 675–688.
- (55) Shinde, P. S.; Lee, S. Y.; Choi, S. H.; Lee, H. H.; Ryu, J.; Jang, J. S. A Synergistic Effect of Surfactant and ZrO₂ Underlayer on Photocurrent Enhancement and Cathodic Shift of Nanoporous Fe₂O₃ Photoanode. *Sci. Rep.* **2016**, *6*, 32436.
- (56) Li, M.; Zhang, J.; Dang, W.; Cushing, S. K.; Guo, D.; Wu, N.; Yin, P. Photocatalytic hydrogen generation enhanced by band gap narrowing and improved charge carrier mobility in AgTaO₃ by compensated co-doping. *Phys. Chem. Chem. Phys.* **2013**, *15*, 16220–16226.
- (57) Green, M. L.; Takeuchi, I.; Hattrick-Simpers, J. R. Applications of high throughput (combinatorial) methodologies to electronic, magnetic, optical, and energy-related materials. *J. Appl. Phys.* **2013**, *113*, 231101.
- (58) Christen, H. M.; Rouleau, C. M.; Ohkubo, I.; Zhai, H. Y.; Lee, H. N.; Sathyamurthy, S.; Lowndes, D. H. An improved continuous compositional-spread technique based on pulsed-laser deposition and applicable to large substrate areas. *Rev. Sci. Instrum.* **2003**, *74*, 4058–4062.
- (59) von Wenckstern, H.; Splith, D.; Werner, A.; Müller, S.; Lorenz, M.; Grundmann, M. Properties of schottky barrier diodes on (In_xGa_{1-x})₂O₃ for 0.01 $\leq x \leq 0.85$ determined by a combinatorial approach. *ACS Comb. Sci.* **2015**, *17*, 710–715.
- (60) Skorupska, K.; Maggard, P. A.; Eichberger, R.; Schwarzburg, K.; Shahbazi, P.; Zoellner, B.; Parkinson, B. A. Combinatorial investigations of high temperature CuNb oxide phases for photoelectrochemical water splitting. *ACS Comb. Sci.* **2015**, *17*, 742–751.
- (61) Hattrick-Simpers, J.; Wen, C.; Lauterbach, J. The materials super highway: integrating high-throughput experimentation into mapping the catalysis materials genome. *Catal. Lett.* **2014**, *145*, 290–298.
- (62) Guevarra, D.; Shinde, A.; Suram, S. K.; Sharp, I. D.; Toma, F. M.; Haber, J. A.; Gregoire, J. M. Development of solar fuels photoanodes through combinatorial integration of Ni–La–Co–Ce oxide catalysts on BiVO₄. *Energy Environ. Sci.* **2016**, *9*, 565–580.
- (63) Woodhouse, M.; Herman, G. S.; Parkinson, B. A. Combinatorial approach to identification of catalysts for the photoelectrolysis of water. *Chem. Mater.* **2005**, *17*, 4318–4324.
- (64) Thienhaus, S.; Naujoks, D.; Pfetzing-Micklich, J.; König, D.; Ludwig, A. Rapid identification of areas of interest in thin film materials libraries by combining electrical, optical, X-ray diffraction, and mechanical high-throughput measurements: a case study for the system Ni-Al. *ACS Comb. Sci.* **2014**, *16*, 686–694.
- (65) Subramaniyan, A.; Perkins, J. D.; O'Hayre, R. P.; Lany, S.; Stevanovic, V.; Ginley, D. S.; Zakutayev, A. Non-equilibrium deposition of phase pure Cu₂O thin films at reduced growth temperature. *APL Mater.* **2014**, *2*, No. 022105.